Heliyon 5 (2019) e03028

Contents lists available at ScienceDirect

Heliyon

journal homepage: www.cell.com/heliyon

Research article

Investigation of the effect of precursor ratios on the solution combustion synthesis of zinc zirconate nanocomposite

M.K. Musembi *, F.B. Dejene

Department of Physics, University of the Free State (Qwa Qwa Campus), Private Bag, X13, Phuthaditjhaba, 9866, South Africa

ARTICLE INFO

Keywords:
Materials chemistry
Materials science
Nanotechnology
Nanocomposite
Zinc zirconate
Solution combustion synthesis
Perovskite
Zirconium butoxide

ABSTRACT

Zinc zirconate nanocomposite was synthesized by a low-temperature solution combustion method using citric acid as fuel at a pH of 7. The synthesis was done by varying the ratios of zirconium butoxide and zinc nitrate, which were the precursors in this study. The samples were calcined at 600 °C for 2 h then their structural and optical characteristics investigated. The analysis showed that the nanocomposite consisted of mixed phases of zinc zirconate, zinc oxide, and zirconium oxide. As the Zn^{2+}/Zr^{4+} ratio increased, the highly agglomerated morphologies gradually developed crystalline aggregates mixed with nanorods. A red-shifted blue emission with a peak at 409 nm was observed in the photoluminescence spectra and the composites had an energy bandgap between 2.81 and 3.12 eV.

1. Introduction

Advancement in nanotechnology has exposed man to a better understanding of the properties of nanomaterials and their applications. The promising research results have encouraged greater depths of exploring a variety of methods of synthesizing semiconductor nanoparticles. Some of the factors that must be considered in choosing a synthesis route are the method's novelty, rate and cost of production as well as the possibility of large-scale production [1, 2].

High-quality powders have been conveniently synthesized by wet chemical methods. Solution combustion synthesis (SCS) is one of the most effective wet chemical methods of synthesizing nanoparticles. In the method, metal nitrates are used alongside suitable amino acids (reducing agent) that act as fuel. SCS involves a self-sustaining exothermic reaction that is usually started off by heating the mixture into self-ignition and makes the method fast, convenient and energy-saving. This route is termed as a low-temperature synthesis because the reactants can be heated using a common table-top hot plate, unlike most solid-state methods that require specialized heating equipment [1, 2, 3, 4, 5].

Among the solar energy technologies, perovskites are among the fastest-growing with their efficiencies having increased from 3.8 % in 2009 to the current 25.2 %, with a possible theoretical efficiency mark of 30 % [6, 7, 8, 9]. Perovskites have a cubic structure of the form ABO_3, where A and B are metals. The perovskite structure is characterized by flexible bond angles that are usually prone to a variety of distortions from the ideal structure. This structure is also found in many high-temperature semiconductors that have three or more metals. In these materials, the oxygen content usually determines the type of ceramic formed ranging from being an insulator to a superconductor [10, 11].

Material scientists have developed a keen interest in the exceptional properties of perovskites. In the microelectronics and telecommunication sectors, perovskites are used in the manufacture of sensors, lasers, fuel cell electrodes, photo-electrolysis and memory devices. Some key aspects of perovskites include their high absorption coefficients as well as the low production cost [10, 12]. Earlier studies have shown that perovskite solar cells face challenges of stability and fast degradation in the environment. Recent studies and research have produced promising results towards the fabrication of commercially viable perovskite solar cells that will probably address these earlier challenges [13, 14].

A lot of research work has been conducted on zinc and zirconium compounds especially their phosphor oxides. Zinc oxide (ZnO) has been widely studied mainly for its applications in solar cells [12, 15]. Zirconium oxide (ZrO_2) being one of the most abundant compounds on the earth's crust and is used in the manufacture of ceramics, dentistry as well as a gemstone due to its high refractive index. ZrO_2 is also used in piezo electronics and as a solid electrolyte in electrochromic devices [16, 17, 18]. Due to the desired optical properties, $ZnZrO_3$ perovskite has been used in photocatalysis and its further development would possibly be useful in the fabrication of PSCs [19].

* Corresponding author.
E-mail address: mchmusembi@yahoo.com (M.K. Musembi).

https://doi.org/10.1016/j.heliyon.2019.e03028
Received 14 October 2019; Received in revised form 29 November 2019; Accepted 9 December 2019

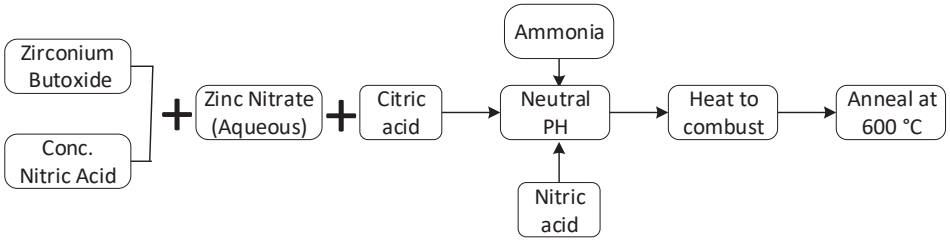

Figure 1. Schematic synthesis for zinc zirconate nanocomposite.

The reaction between two or more constituent materials with different physical or chemical properties produces a composite material whose characteristics are significantly different from those of the constituents. These composite materials have demonstrated enhanced optical properties and better stability in comparison with the single-phase constituent materials [20]. This study sought to synthesize zinc zirconate nanocomposite by a less traditional route involving solution combustion, then investigate its structural and optical characteristics. To the best of our knowledge, there is no report on the use of the SCS method in the synthesis of zinc zirconate nanocomposites. Further, there is no study that has reported the use of zirconium butoxide as a precursor in the synthesis of the nanocomposite.

2. Materials and methods

The zinc zirconate composite was prepared using analytical grade zinc nitrate from Merck and zirconium butoxide from Aldrich. Citric acid, nitric acid, and ammonia of analytical grade from Merck were also used. The synthesis was carried out by oxidizing 1.0 ml of zirconium (IV) butoxide with 2.677ml of concentrated nitric acid and the explosive reaction allowed to complete in an Alphalab fume chamber. 50 ml of water were added and the solution was magnetically stirred for 30 min. Eight such solutions were mixed with varying amounts of zinc nitrate dissolved in 50 ml of water. 1 g of citric acid was added into each solution then the pH adjusted to 7 using ammonia solution. The mixtures were stirred continuously for 1 h then heated to self-combustion using a Labcon hot plate, model MSH10. Each of the resulting powders was crushed then calcined at 600 °C for 2 h, a temperature observed by Ramos-Guerra et al [21] to produce better crystallinity especially for the ZrO_2 phase.

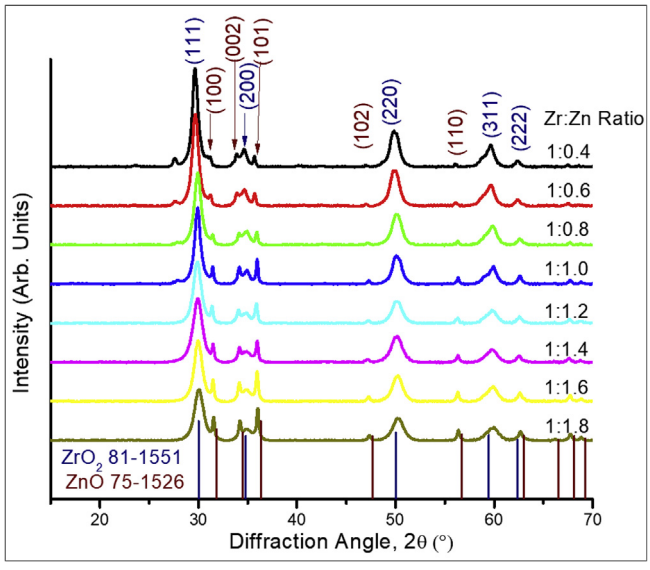

Figure 2. The XRD patterns of the samples prepared using different precursor ratios against the matching ZnO (brown) and ZrO_2 (navy blue) reference files.

Figure 1 illustrates the synthesis method used in this study. The properties of the nanocomposite powders were investigated using various characterization techniques. X-ray diffraction (XRD) data were collected using a Phillips Bruker D8 X-ray diffractometer with CuKα radiation of 0.1506 nm at a scan speed of 0.012 per min in steps of 0.01° between 10° and 70°. Scanning electron microscopy (SEM) characterization was done using Jeol JSM-7800F Field Emission SEM equipped with Oxford Aztec EDS and Gatan Mono CL4 while a Philips CM 100 system was used for transmission electron microscopy (TEM). Diffuse reflectance was obtained using a Lambda 950 PerkinElmer UV WinLab Spectrometer within the wavelength range of 200 and 800 nm. The photoluminescence (PL) characteristics were determined using a Hitachi Model F-7000 FL Spectrophotometer fitted with a xenon lamp within the range of 200–1000 nm.

3. Results and discussion

3.1. Structural analysis of the composite by X-ray diffraction

Figure 2 shows the diffraction patterns of the annealed composite samples. The patterns were deconvoluted using Fityk software [22] and collated in order to establish independent peak profiles for each of the phases in the composite in order to determine profile characteristics. For each phase, the first three major peaks were used in this investigation. The material was identified by comparing the XRD patterns with the existing International Centre for Diffraction Data (ICDD) reference files. The process revealed mixed phases of cubic zirconium oxide and hexagonal zinc oxide nanocrystallites as inferred from ICDD cards 81–1551 and 75–1526 respectively. In the samples prepared using higher ratios of Zr^{4+} ions, an emerging zinc zirconate perovskite peak inferred from card 32–1482 was observed at an angle of 28.2°. The identification of all the major diffraction peaks that were observed is an indication of the purity of the synthesized nanoparticles.

The use of different precursor ratios produced similar patterns with slight variations in the peak positions, their intensities as well as the width, leading to different crystalline features. The peaks were generally broad indicating the formation of nano-range particles and were in agreement with those obtained in similar studies [19, 23].

Table 1. ZrO_2 crystal characteristics.

XRD Analysis for ZrO_2				
Sample Zr: Zn	Average D, nm	Strain ε $\times 10^{-3}$	Average d, (Å)	Lattice constant a (Å)
1 : 0.4	19.24	4.783	2.079	5.052
1 : 0.6	17.15	5.346	2.079	5.052
1 : 0.8	16.49	5.526	2.066	5.025
1 : 1.0	18.54	4.938	2.066	5.024
1 : 1.2	15.11	6.054	2.068	5.028
1 : 1.4	13.93	6.659	2.066	5.025
1 : 1.6	15.35	5.957	2.063	5.017
1 : 1.8	13.63	6.709	2.059	5.011

Table 2. Crystallite properties of the deconvoluted ZnO peak profiles.

ZnO XRD Analysis					
Sample Zr: Zn	Average D, nm	Strain $\varepsilon \times 10^{-3}$	Average d, (Å)	Lattice Constants a b (Å)	
1 : 0.4	47.75	1.808	1.814	3.088	5.349
1 : 0.6	56.44	2.123	2.610	3.125	5.413
1 : 0.8	64.63	1.812	2.593	3.105	5.378
1 : 1.0	57.16	1.717	2.224	3.121	5.406
1 : 1.2	46.29	2.169	2.224	3.127	5.415
1 : 1.4	56.49	1.791	2.268	3.178	5.505
1 : 1.6	53.44	2.226	2.591	3.103	5.374
1 : 1.8	54.25	2.174	2.586	3.096	5.362

The Scherrer Eq. (1) [16, 24] and the Delft model Eq. (2) for sample broadening [25] were used on each of the peak profiles to determine the crystallite size and strain respectively.

$$\text{Crystal size, } D = \frac{k\lambda}{\beta \cos\theta} \tag{1}$$

$$\text{Crystal strain, } \varepsilon = \frac{\beta}{4 \tan\theta} \tag{2}$$

where D is the crystal size, β is the peak broadening of full width at half maximum (FWHM), λ is the wavelength of X-ray radiation used (1.5406 Å), while θ is the Bragg's diffraction angle and k is a dimensionless constant that is dependent on the shape of the crystallites.

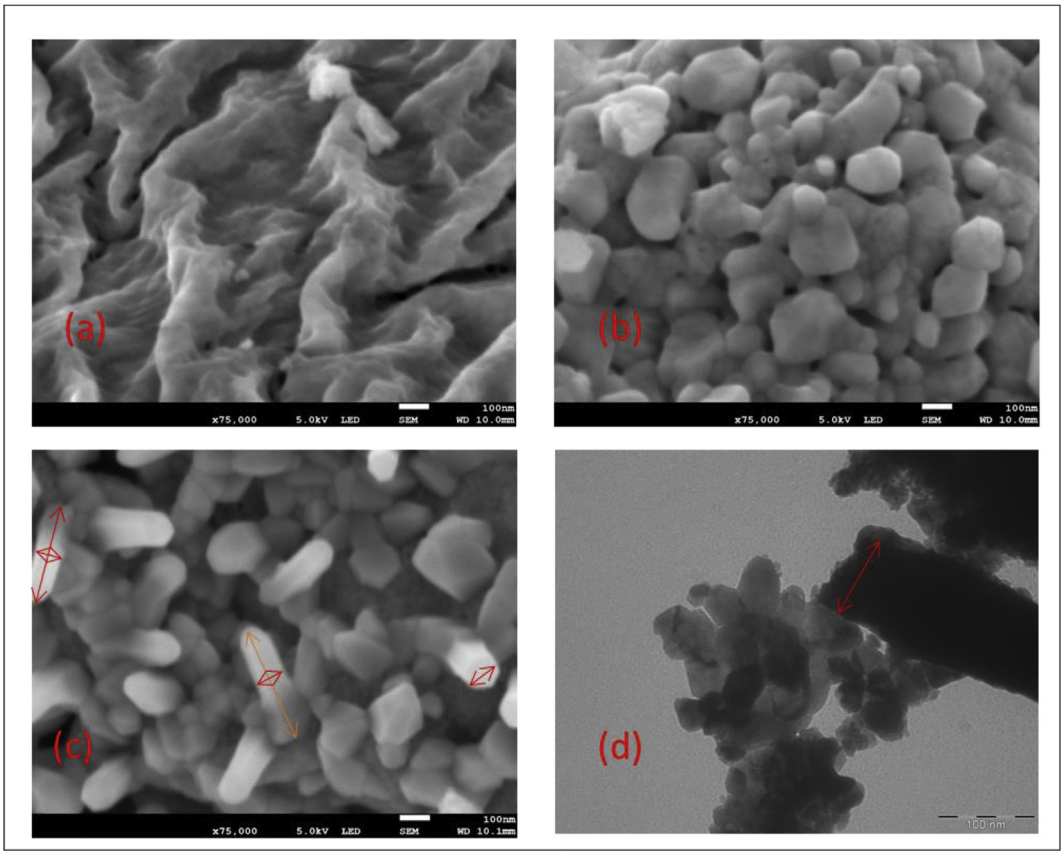

Figure 3. SEM images at (a) Zr: Zn = 1: 0.6 (b) Zr: Zn = 1: 1 (c) Zr: Zn = 1: 1.6 precursor ratio 3(d) TEM image showing crystallites and nanorods at Zr: Zn = 1: 1.6 precursor ratio. The size of the rods in (b) and (c) had average dimensions of 350 by 100 nm.

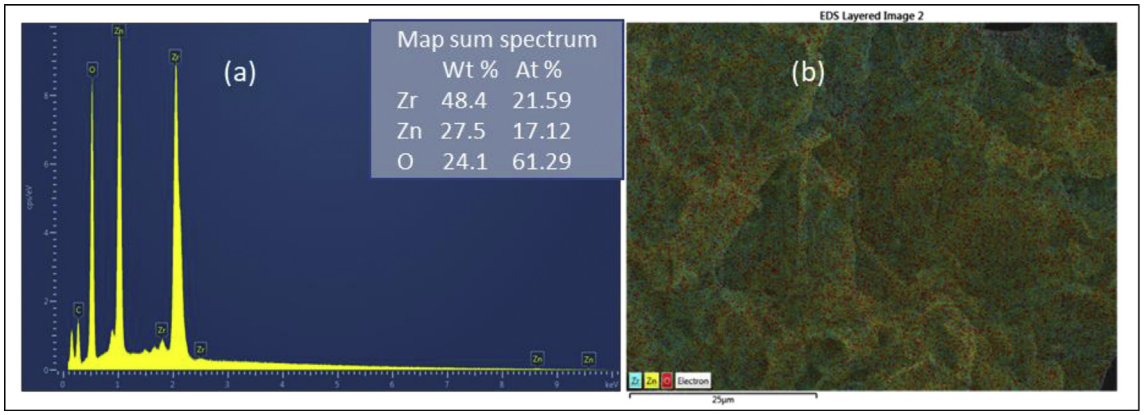

Figure 4. (a) The elemental composition (b) spectrum map at Zr: Zn = 1: 1 precursor ratio.

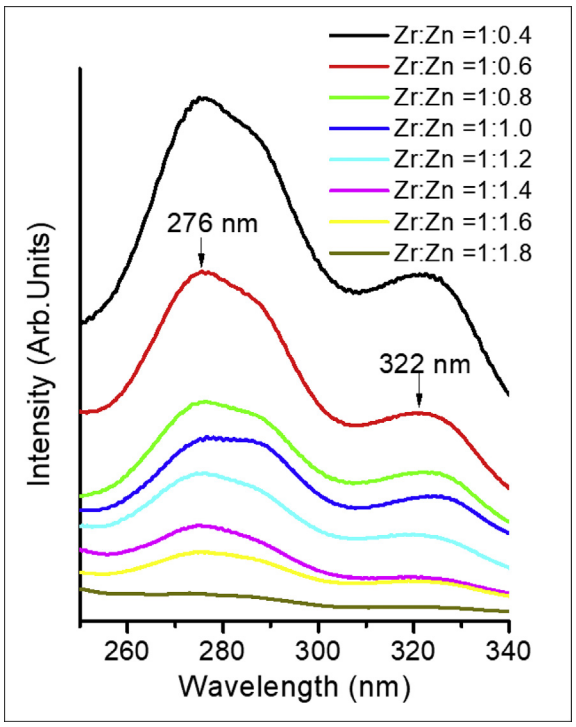

Figure 5. The excitation spectra peaks of the nanocomposite at 413 nm.

The Bragg's equation, $n\lambda = 2d\,sin\theta$ was used to determine the interplanar spacing, *d*. The lattice parameters of crystals were calculated depending on the crystalline structure of that phase of the material [26].

Table 1 presents the characteristics of cubic ZrO_2 crystals. The major crystal planes of the zirconia phase that corresponded to (111), (220) and (311) were observed around 30°, 50°, and 60° respectively. From the figure, the ZrO_2 peak intensities were seen to increase with enhanced Zr^{4+} ion concentration. There was a general shift in the peak positions towards longer wavelengths and a decrease in the crystallite size of the zirconia nanoparticles as the Zn^{2+}/Zr^{4+} ratio increased. This was associated with a slight decrease in the interplanar spacing *d* as well as the corresponding lattice constant *a*, as illustrated in Table 1. The average values obtained in this study for *d* and *a* were 2.07 Å and 5.03 Å respectively, which are slightly smaller than 5.152 Å of the bulk zirconia. Such a deviation was attributed to the presence of micro-strains in the particles or the influence of the solid solutions formed within the mixture.

Table 2 shows the properties of the hexagonal ZnO phase. The (101) plane around 36° was the most distinct ZnO peak in the material. For the second and third peaks, there were a gradual shift in the preferential orientation between the (103), (110), (100), (002) planes as the Zn^{2+}/Zr^{4+} ratio increased. Comparatively, the intensities of ZnO peaks were seen to increase with the enhanced concentration of the Zn^{2+} ions as more particles get preferentially aligned within those planes.

It was noticed that there was a general shift of the position of the peaks towards longer wavelengths as the Zn^{2+}/Zr^{4+} ratio was increased. This was characterized by an increasing trend in the FWHM of the peaks and an associated decrease in the crystallite sizes of the nanoparticles. The average values obtained for *d*, *a* and *c* were 2.36, 3.12 and 5.40 Å respectively; which was a slight variation from the reference 3.22 and 5.20 Å for *a* and *c* respectively.

3.2. Morphology and compositional analysis

Figure 3(a-c) shows selected SEM images of the nanocomposite. From the micrographs, it is observed that the texture and surface features of the nanocomposites were heavily dependent on the ratio of the precursors used in the synthesis.

At a lower concentration of Zn^{4+} ions, the micrograph in Figure 3(a) shows a highly agglomerated spongy surface. It depicts uneven branched formations characterized by rough texture. Figure 3(b) displays a crystalline material of high porosity in which the particles are better aggregated as compared to samples with lower ratios of Zr^{4+}. The morphology of the sample in Figure 3(c) shows a further reduction in the density of agglomerates and enhanced crystallinity with the increasing percentage of the Zr^{4+} with nanorod formations.

Figure 3(d) shows a selected TEM image of the nanocomposite. In the micrograph, the cubic and hexagonal structures, as well as nanorods, are

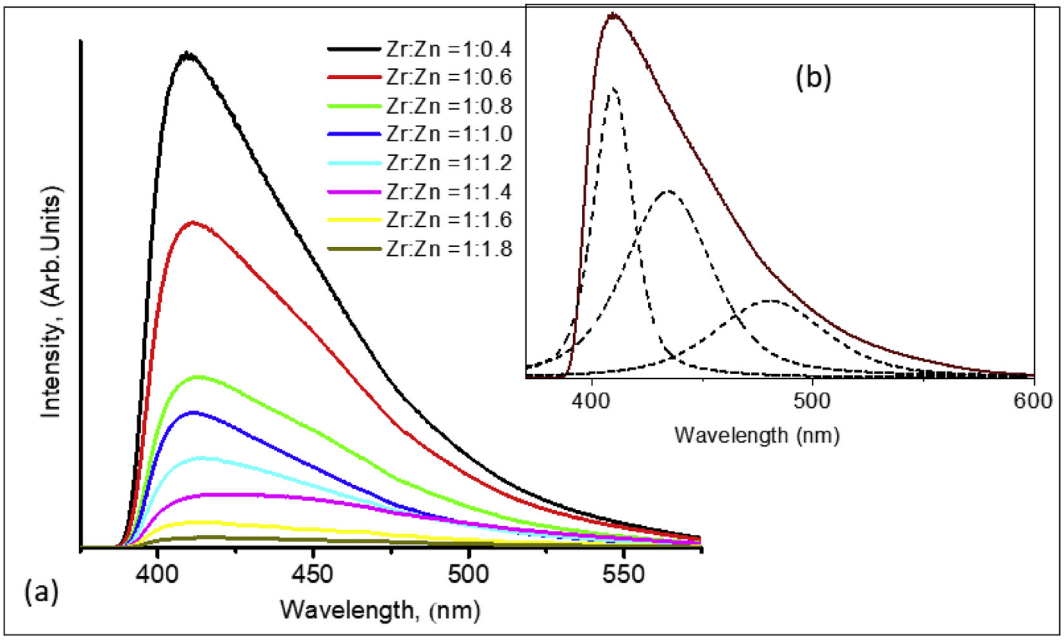

Figure 6. (a) Emission spectrum of the composite at varying ratios of the precursors while inset (b) is the deconvoluted Zr:Zn = 1:0.4 profile showing peaks at 409, 434 and 480 nm.

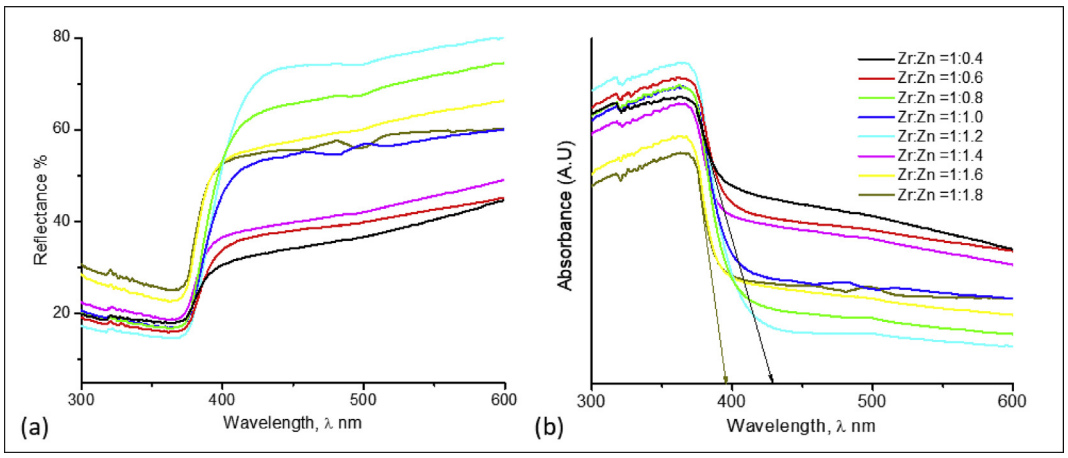

Figure 7. (a) UV percentage reflectance (b) absorbance spectra showing the range absorption edges in the composite.

seen confirming the polycrystalline nature of the nanocomposite. The average dimensions of the nanorod particles as determined by both SEM and TEM were about 350 nm by 100 nm. Comparing these dimensions with the crystallite sizes in Tables 1 and 2, it was concluded that the particles were indeed polycrystalline.

Figure 4 (a) shows the elemental composition of one of the samples. The results established Zn, Zr and O peaks in the spectra confirming the presence of elements in a fair stoichiometric ratio. From the maps, it was seen that there is no other element present in the composite, apart from the carbon coating used in the sample preparation film. The micrograph in Figure 4(b) further shows that there was a fair and homogeneous distribution of the elements within the composite.

3.3. Optical properties from photoluminescence analysis

Figure 5 shows the excitation spectra of the nanocomposites. The samples exhibited a prominent excitation peak at 276 nm and a minor one at 322 nm. These excitation peaks had a reduced intensity as the concentration of Zn^{2+} ions increased, leading to the conclusion that they must be originating from the ZrO_2 in the matrix. The material was probed at 276 nm and the emission spectra, whose prominent peak was observed at 409 plotted in Figure 6. This prominent peak was attributed to the band to band transition of ZrO_2 within the composite. There were variations both in shape, intensity and peak position in the spectra depending on the ratio of the precursors. For the samples synthesized using a higher Zr^{4+} ion concentration, the emission peaks were sharper, more intense and red-shifted. These peaks broadened towards longer wavelengths due to the emergence of other peak profiles as the ratio of the Zn^{2+} ions increased, with the broadening associated with absorptions due to charge transfer within the composite

The inset in Figure 6 shows a deconvoluted profile at 409 nm which depicted other minor emission peaks around 434 and 480 nm [27, 28]. According to Selvam et al [29], these emissions are associated with deep traps arising from electron-hole pair recombination found deep inside the energy bandgap. These peaks became more dominant as the concentration of Zn^{2+} ions increased, indicating a higher density of defects or oxygen vacancies in ZnO within the matrix.

3.4. UV-vis analysis

Metals are known to have a high reflectance in the infrared region, which reduces relatively in the visible range and absorb radiations past the plasma frequency [30]. Figure 7(a) shows the UV reflectance spectrum of the composite. There were minor absorption peaks around 320 nm as reported by Ivanova et al [31] which they attributed to excitonic transitions in the mixed phases. By extrapolating the straight sections of the sharply falling absorbance curves in Figure 7(b), the absorption edges of the composite were determined. These edges stretched more into the longer wavelengths than those reported by Xinhua Zhu et al [32], by extending from 394 nm up to 427 nm, with a minor one around 500 nm whose intensity increased with enhanced Zn^{2+} ions as observed in the PL analysis. There is a significant red-shift in the absorption edges as the Zn^{2+}/Zr^{4+} ratio increased.

An increase of the photon energy beyond the energy bandgap of a semiconductor promotes most of the electrons into the conduction band causing a sudden increase in the absorbance. The reflectance of the composite is relatively high for wavelengths above 409 nm since the photon-energy is unable to excite many electrons into the conduction band.

Using the Kubelka-Munk function, the energy bandgap was determined as illustrated in Figure 8. It was found that the energy bandgap lies between 2.81 and 3.12 eV, which is in the same range as that obtained in other studies [23, 32]. The figure shows that there was a general decrease of the energy bandgap with increasing Zn^{2+}/Zr^{4+} precursor ratios which is an advantage that composites have over any of the single-phase constituent materials. The energy band gaps of the nano-powders can, therefore, be conveniently tuned by varying the Zn^{2+}/Zr^{4+} precursor

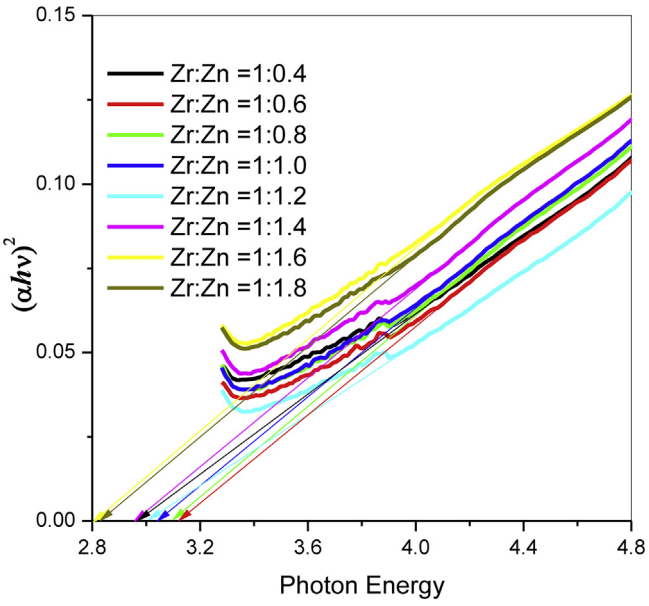

Figure 8. Kubelka-Munk function of the composite for determining energy bandgap.

ratios. The synthesized nanocomposite can as well be used in the photocatalytic treatment of water and the removal of dyes [19, 33].

4. Conclusion

The solution combustion route was successfully used to synthesize a nanocomposite consisting of mixed phases of zinc oxide, zirconium oxide, and zinc zirconate nanoparticles. As the Zn^{2+} ion concentration increased, the highly agglomerated morphologies gradually developed crystalline aggregates mixed with nanorods, while the intensity of the major emission peak at 409 nm decreased. Depending on the composition of the nanocomposites, there was a tunable energy bandgap ranging from 2.81 and 3.12 eV. The study, therefore, showed that the nanocomposite properties can be influenced through the control of the precursor ratios. If these blue-emitting phosphors are doped with rare earth metals, the nanocomposites can be used within a wide range of photon energies in efficient white-light-emitting applications. A further investigation of the synthesis parameters like the pH, fuel and synthesis temperature is needed so as to enhance the yield of the $ZnZrO_3$ perovskite phase for possible application in solar cells.

Declarations

Author contribution statement

F. Dejene: Conceived and designed the experiments; Analyzed and interpreted the data; Contributed reagents, materials, analysis tools or data.

M. Michael: Performed the experiments; Analyzed and interpreted the data; Wrote the paper.

Funding statement

This work was supported by the National Research Fund, NRF S.A.

Competing interest statement

The authors declare no conflict of interest.

Additional information

No additional information is available for this paper.

Acknowledgements

The authors wish to thank Dr. Iokyaa Ahemen and Dr. Obi Kingsley for the continued advice received during the work.

References

[1] A.K. Alves, C.P. Bergmann, F.A. Berutti, Novel synthesis and characterization of nanostructured materials, in: Combustion Synthesis, Springer-Verlag Berlin Heidelberg, 2013, pp. 11–20.
[2] R. Jose Varghese, E.h.M. Sakho, S. Parani, S. Thomas, O.S. Oluwafemi, J. Wu, Introduction to nanomaterials: synthesis and applications. Nanomaterials for solar cell applications, in: Nanomaterials for Solar Cell Applications, first ed., Elsevier, 2019, pp. 75–95.
[3] A.L.S.-L. Thomas, Solution combustion synthesis of oxide semiconductors, PhD Thesis, The University of Texas Arlington, 2015.
[4] Arvind Varma, A.S. Mukasyan, A.S. Rogachev, K.V. Manukyan, Solution combustion synthesis of nanoscale materials, Chem. Rev. 116 (2016) 14493–14586.
[5] A.S. Mukasyan, P. Epstein, P. Dinka, Solution combustion synthesis of nanomaterials, Proc. Combust. Inst. 31 (2007) 1789–1795.
[6] A. Kojima, K. Teshima, Y. Shirai, T. Miyasaka, Organometal halide perovskites as visible-light sensitizers for photovoltaic cells, J. Am. Chem. Soc. 131 (2009) 6050–6051.
[7] J.-P. Correa-Baena, A. Abate, M. Saliba, W. Tress, T.J. Jacobsson, M. Grätzelc, et al., The rapid evolution of highly efficient perovskite solar cells, Energy Environ. Sci. 10 (2017) 710–727.
[8] J.S. Manser, J.A. Christians, P.V. Kamat, Intriguing optoelectronic properties of metal halide perovskites, Chem. Rev. 116 (2016) 12956–13008.
[9] K.A. Emery, Best research-cell efficiency chart, 01/10/2019. https://www.nrel.gov/pv/assets/pdfs/best-research-cell-efficiencies.20190802.pdf.
[10] W.-J. Yin, T. Shi, Y. Yan, Unique properties of halide perovskites as possible origins of the superior solar cell performance, Adv. Mater. 26 (2014) 4653–4658.
[11] V.C. Milos Petrovic, Seeram Ramakrishna, Perovskites: solar cells & engineering applications – materials and device developments, Sol. Energy 122 (2015) 678–699.
[12] R. Vittala, K.C. Ho, Zinc oxide based dye-sensitized solar cells: a review, Renew. Sustain. Energy Rev. 70 (2017) 920–935.
[13] J. Tong, Z. Song, A.F. Palmstrom, O.G. Reid, G. Teeter, M.C. Beard, et al., Carrier lifetimes of >1 μs in Sn-Pb perovskites enable efficient all-perovskite tandem solar cells, Science 364 (6439) (2019) 475–479.
[14] G. Grancini, C. Roldán-Carmona, I. Zimmermann, E. Mosconi, X. Lee, D. Martineau, et al., One-Year stable perovskite solar cells by 2D/3D interface engineering, Nat. Commun. 8 (2017).
[15] V. Sugathan, E. John, K. Sudhakar, Recent improvements in dye sensitized solar cells: a review, Renew. Sustain. Energy Rev. 52 (2015) 54–64.
[16] I. Ahemen, F.B. Dejene, Photophysical and energy transfer processes in Ce^{3+} co-doped ZrO2: Eu^{3+} nanorods, Appl. Phys. A 123 (2017).
[17] I. Ahemen, F.B. Dejene, Spectroscopic investigation of Ce^{3+}/Eu^{3+} co-doped Li_2BaZrO_4 nanocrystalline phosphors, J. Alloy. Comp. 735 (2017) 2436–2445.
[18] R. Nielsen, T. Chang, in: Zirconium and Zirconium Compounds, Wiley-VCH Verlag GmbH & Co. KGaA, Weinheim, 2005, pp. 2–17.
[19] M.H. Habibi, E. Askari, Preparation of a novel zinc zirconate nanocomposite coated on glass for removal of a textile dye (reactive brilliant red X8B) from water, Synth. React. Inorg. Metal-Org. Nano-Metal Chem. 45 (2015) 1457–1462.
[20] D.S.-. Mathur, M. Veith, H. Shen, S. Hüfner, Single-step preparation of nanosized ceramics and composites from metal-organic precursors, in: 26th Annual Conference on Composites, Advanced Ceramics, Materials, and Structures: B: Ceramic Engineering and Science Proceedings, 2008, pp. 557–568.
[21] A.I. Ramos-Guerra, J. Guzmán-Mendoza, M. García-Hipólitob, O. Alvarez-Fregoso, C. Falconyc, Multicolored photoluminescence and structural properties of zirconium oxide films co-doped with Tb^{3+} and Eu^{3+} ions, Ceram. Int. 41 (2015) 11279–11286.
[22] M. Wojdyr, Fityk: a general-purpose peak fitting program, J. Appl. Cryst. 43 (2010) 1126–1128.
[23] M.H. Habibi, E. Askari, Fabrication and spectral properties of zinc zirconate nanorod composites by sol-gel method for optical applications: effect of chloride and oxychloride precursors and sintering temperature on band gap, Synth. React. Inorg. Metal-Org. Nano-Metal Chem. 45 (2015) 281–285.
[24] F.T.L. Muniz, M.A.R. Miranda, C. Morilla dos Santos, J.M. Sasaki, The Scherrer equation and the dynamical theory of X-ray diffraction, Acta Crystallographica Section A Foundations and Advances 72 (2016) 385–390.
[25] N.S. Gonçalves, J.A. Carvalho, Z.M. Lima, J.M. Sasaki, Size–strain study of NiO nanoparticles by X-ray powder diffraction line broadening, Mater. Lett. 72 (2012) 36–38.
[26] Arkajit, Arghya, Sucharita, Tarit, Solid State Calistry Calculator, 2015. https://calistry.org/solid-state.
[27] N. Padmavathy, R. Vijayaraghavan, Enhanced bioactivity of ZnO nanoparticles—an antimicrobial study, Sci. Technol. Adv. Mater. 9 (2008).
[28] O. Yayapao, T. Thongtemb, A. Phuruangrat, S. Thongtem, Sonochemical synthesis of Dy-doped ZnO nanostructures and their photocatalytic properties, J. Alloy. Comp. 576 (2013) 72–79.
[29] N.C.S. Selvam, J.J. Vijaya, L.J. Kennedy, Effects of morphology and Zr doping on structural, optical, and photocatalytic properties of ZnO nanostructures, Ind. Eng. Chem. Res. 51 (2012) 16333–16345.
[30] S.A. Maier, Plasmonics: Fundamentals and Applications, 2007, pp. 11–30, 25/06/2019.
[31] T. Ivanova, A. Harizanova, T. Koutzarova, B. Vertruyen, Effect of annealing temperatures on properties of sol-gel grown ZnO-ZrO2 films, Cryst. Res. Technol. 45 (2010) 1154–1160.
[32] X. Zhu, J. Zhou, J. Zhu, Z. Liu, Y. Li, T. Al-Kassab, Structural characterization and optical properties of perovskite $ZnZrO_3$ nanoparticles, J. Am. Ceram. Soc. 97 (2014) 1987–1992.
[33] S. Aghabeygi, M. Khademi-Shamami, ZnO/ZrO2 nanocomposite: sonosynthesis, characterization and its application for wastewater treatment, Ultrason. Sonochem. 41 (2018) 458–465.